This journal is © The Royal Society of Chemistry 2025

$Ti_3C_2T_x$ and $Mo_2TiC_2T_x$ MXene-based biocompatible supercapacitors for implantable medical devices

Dhrubajyoti Chowdhury[1 a], Sreejesh Moolayadukkam[2,3 a], Priyankan Datta[2], Ishwar K. Puri[1,2,4*]

[1]Mork Family Department of Chemical Engineering and Material Science, University of Southern California, Los Angeles, CA 90089, United States
[2]Department of Aerospace and Mechanical Engineering, University of Southern California, Los Angeles, CA 90089, USA
[3]Iovine and Young Academy, University of Southern California, Los Angeles, CA 90089, United States
[4]Alfred E. Mann Department of Biomedical Engineering, University of Southern California, Los Angeles, CA 90089, United States
[a]Equal contribution

**Corresponding author: ikpuri@usc.edu*

Calculations of c-lattice parameter (c-LP) from XRD plots

The XRD plots were used to identify the crystalline peaks for both S-MXene and D-MXene. At the (002) peak of S-MXene and D-MXene, the c-lattice parameter (c-LP) is calculated to confirm its expansion compared to the c-LP of S-MAX and D-MAX.

The c-lattice parameter (c-LP) is calculated as twice the amount of d-spacing at (002) peak position (d_{002}) as described in the following equation,[1,2] i.e.,

$$n\lambda = 2d_{002}sin2\theta \tag{1}$$

$$c - LP = 2d_{002} \tag{2}$$

where n denotes an integer (usually taken as 1), λ wavelength of incident X-ray beam (1.54Å), d_{002} d-spacing in the (002) plane, 2θ angle of diffraction, $c - LP$ c-lattice parameter.

Williamson-Hall analysis from XRD plots

The lattice micro-strain has been studied using the Williamson-Hall analysis. As per equation 3,[3] the slope of β cos(θ) and 4sin(θ) gives us the value of ε, which is the lattice micro-strain.

$$\beta \cos(\theta) = \frac{K\lambda}{D} + 4\varepsilon \sin(\theta) \tag{3}$$

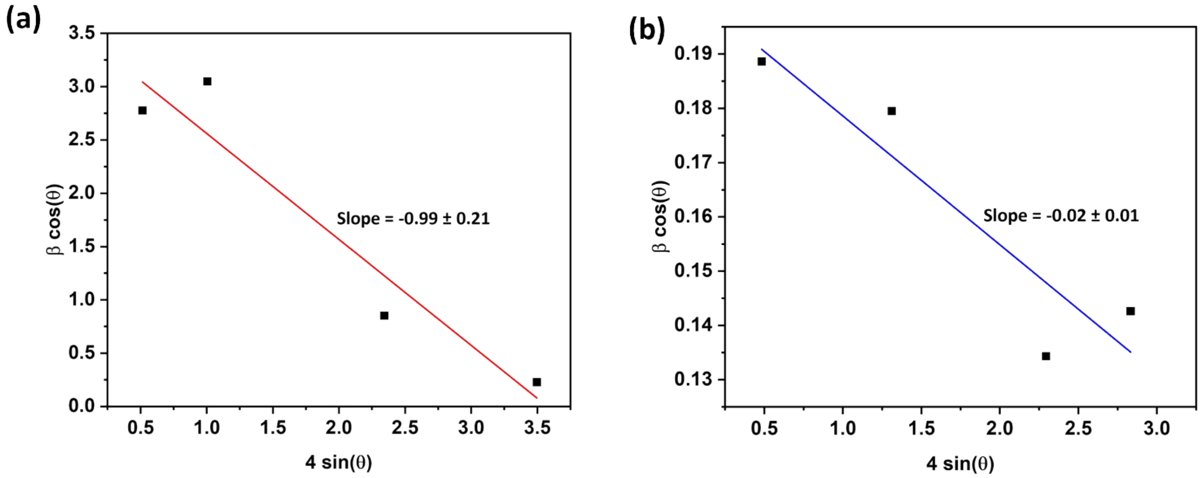

Figure S1. Williamson-Hall analysis of a) S-MXene and b) D-MXene, where the negative slope indicates compressive lattice micro-strain.

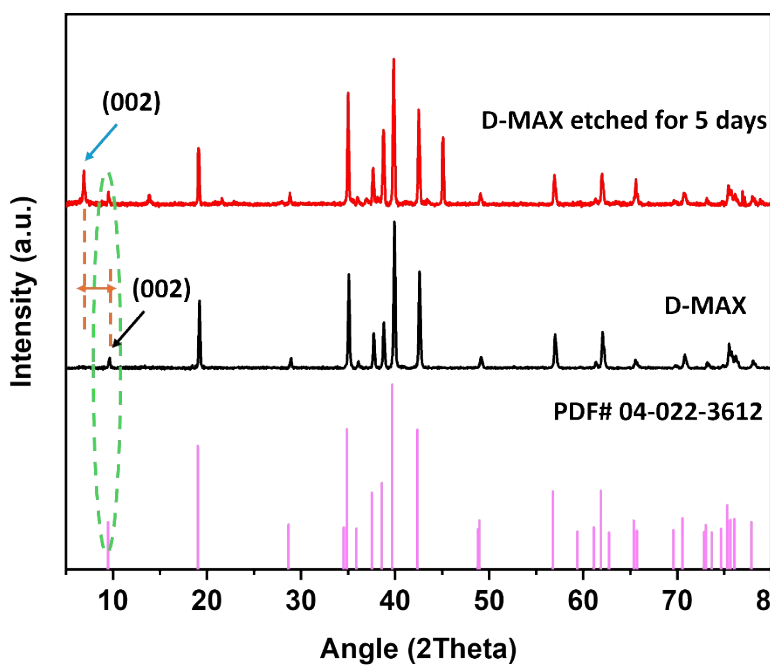

Figure S2. X-ray diffraction (XRD) image of D-MAX initially etched for 5 days, where D-MAX persists

Table S1. c-LP calculation for S-MXene and D-MXene

Material	The angular position of (002) peak (°)	c-LP (Å)
S-MXene	7.35	12.05
D-MXene	6.90	12.83

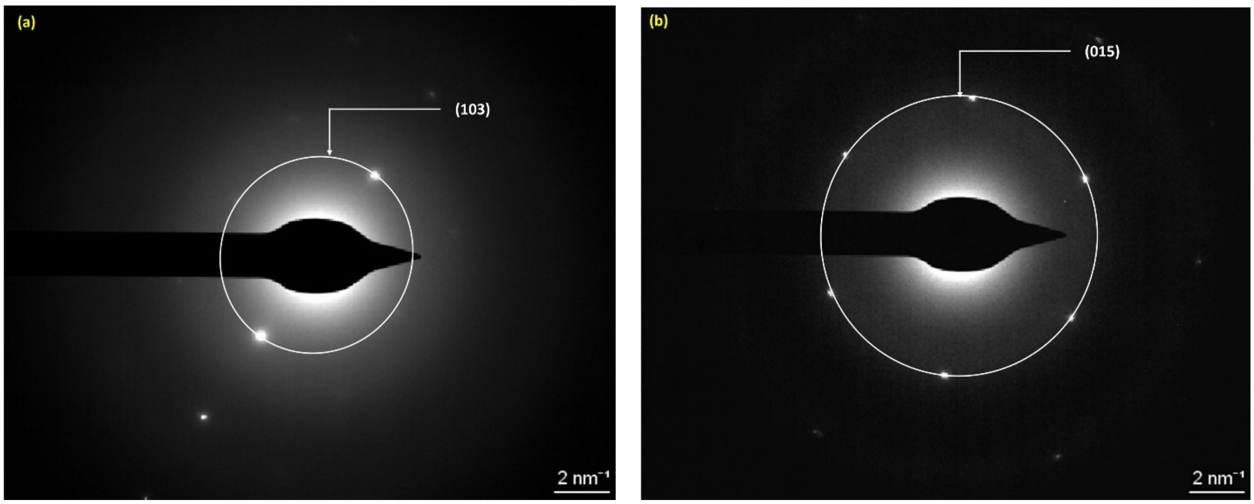

Figure S3. Selected area diffraction (SAED) pattern for a) S-MXene and b) D-MXene, where both MXenes show their corresponding crystalline plane.

Table S2. Calculation for the crystalline plane observed from SAED

Material	Diameter of the circle (1/D) (1/nm)	d -spacing measured from SAED = Radius of the circle (r) (nm)	Corresponding peak measured from XRD (°)	Crystalline plane observed in SAED pattern
S-MXene	7.44	~0.26nm	33.7	(220)
D-MXene	10.12	~0.19nm	44.7	(015)

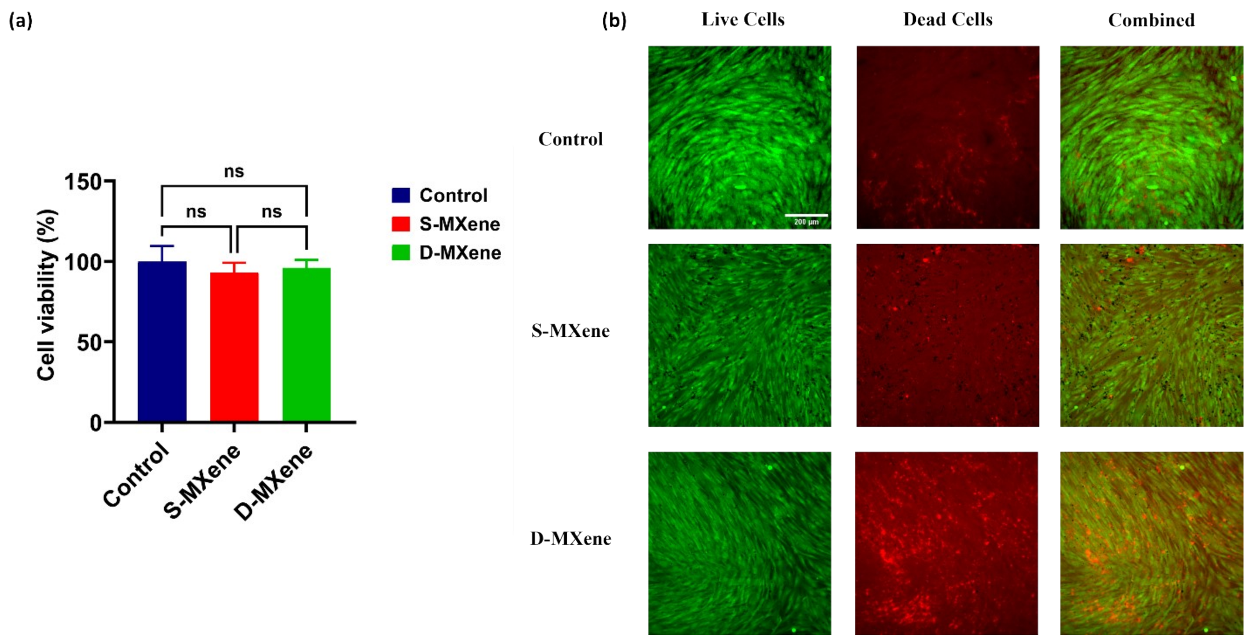

Figure S4. a) Human dermal fibroblast (HDF) cell viability (%) for both MXenes, b) Fluorescence images of live and dead cells for the control group, S-MXene, and D-MXene. After 24 h of incubation in the presence of both MXenes (30 µg ml^{-1}), cells are co-stained with Calcein AM and BOBO 3 iodide and incubated for 15 min. Images are obtained with a Lecia Microsystem Inc. microscope using a standard FITC/Texas Red filter (488/570). S-MXene and D-MXene have no significant effect on cell viability, confirming the biocompatibility of both MXenes.

Table S3. Cell viability (%) of control, S-MXene and D-MXene when incubated for 5 days (120 h)

Sample	**Cell viability (%)**
Control	112.9 ± 7.58
S-MXene	97.34 ± 11.04
D-MXene	107.1 ± 6.179

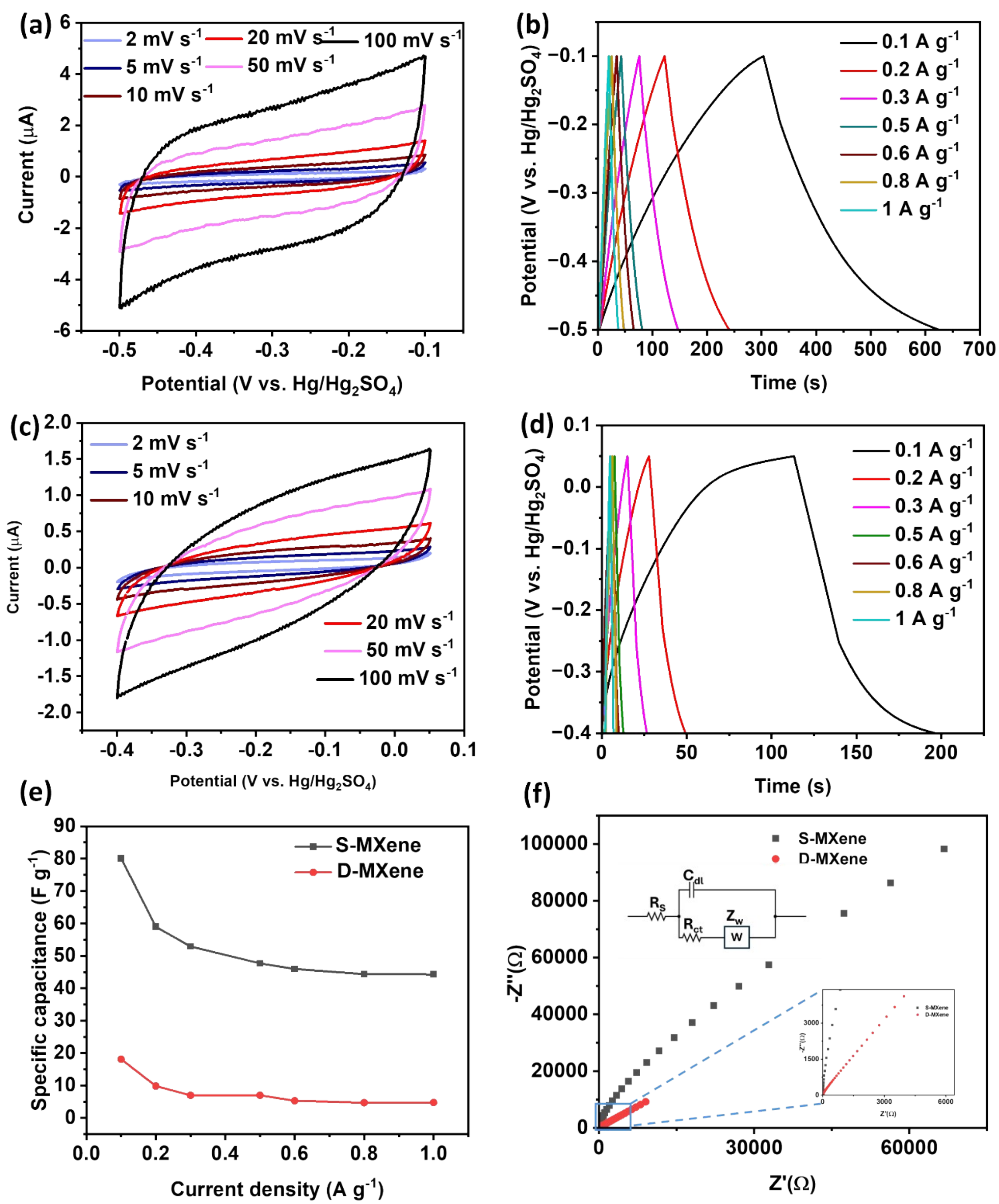

Figure S5. Electrochemical performance of S-MXene and D-MXene in 1 M H_2SO_4 solution. Electrochemical performance of S-MXene a) CV at 2, 5, 10, 20, 50, and 100 mV/s scan rates, b) GCD plots measured at 0.1, 0.2, 0.3, 0.5, 0.6, 0.8 and 1 A g^{-1} current densities, electrochemical performance of D-MXene c) CV at 2, 5, 10, 20, 50, and 100 mV s^{-1} scan rates, d) GCD plots measured at 0.1, 0.2, 0.3, 0.5, 0.6, 0.8 at 1 A g^{-1} current densities, and e) specific capacitance comparison of S-MXene and D-MXene. The GCD plots were used to calculate specific capacitance for the MXene, and f) Electrochemical impedance spectroscopy (EIS) of S-MXene and D-MXene MXenes in 1 M H_2SO_4 electrolyte, (inset) the circuit used for modeling, where R_s: solution resistance, C_{dl}: double layer capacitance at the electrode surface, R_{ct}: charge transfer resistance, Z_w: Warburg resistance. Higher charge transfer resistance (R_s) was obtained for D-MXene, while S-MXene displayed higher capacitance. The GCD plots were used to calculate specific capacitance for both the MXenes. S-MXene showed superior performance.

Table S4. Summary of the C_{sp} values obtained for the different electrolytes for both S-MXene and D-MXene

	Material			
Electrolyte	**S-MXene**		**D-MXene**	
1 M H_2SO_4	**Current density ($A\ g^{-1}$)**	**C_{sp} ($F\ g^{-1}$)**	**Current density ($A\ g^{-1}$)**	**C_{sp} ($F\ g^{-1}$)**
	0.1	80.12	0.1	18.33
	0.2	59.98	0.2	9.83
	0.3	52.91	0.3	6.97
	0.5	47.69	0.5	7.00
	0.6	45.98	0.6	5.29
	0.8	44.36	0.8	4.71
	1.0	44.30	1.0	4.77
1 M Na_2SO_4	**Current density ($A\ g^{-1}$)**	**C_{sp} ($F\ g^{-1}$)**	**Current density ($A\ g^{-1}$)**	**C_{sp} ($F\ g^{-1}$)**
	0.1	34.76	0.1	1.39
	0.2	22.18	0.2	0.47
	0.3	20.96	0.3	0.48
	0.5	20.42	0.5	1.16
	0.6	18.08	0.6	0.71
	0.8	20.54	0.8	0.80
	1.0	19.41	1.0	0.81
	Current density ($A\ g^{-1}$)	**C_{sp} ($F\ g^{-1}$)**	**Current density ($A\ g^{-1}$)**	**C_{sp} ($F\ g^{-1}$)**

PBS	0.1	38.37	0.1	7.25
	0.2	27.91	0.2	4.66
	0.3	26.24	0.3	3.74
	0.5	26.16	0.5	3.06
	0.6	24.57	0.6	2.93
	0.8	25.96	0.8	2.35
	1.0	26.90	1.0	2.66

Table S5. EIS data obtained for both S-MXene and D-MXene in 1 M H_2SO_4

	Material	
Component values obtained	**S-MXene**	**D-MXene**
R_s	6.24 Ω	13.9 Ω
C_{dl}	3.56 µF	1.74 µF
R_{ct}	5 Ω	3.18 µΩ
Z_w	8.44 nMhos$^{1/2}$	96.7 nMhos$^{1/2}$

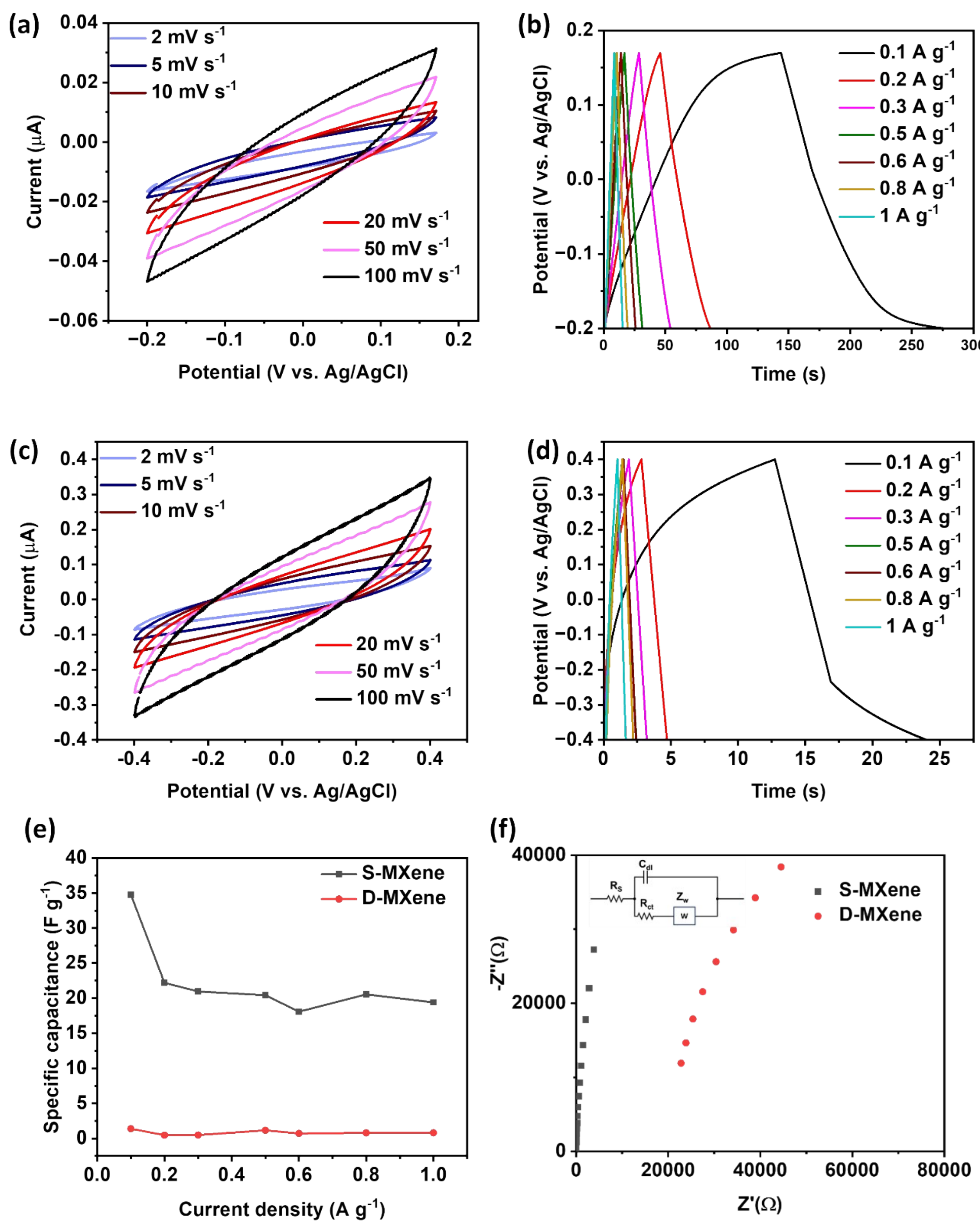

Figure S6. Electrochemical performance of S-MXene and D-MXene in 1 M Na_2SO_4 solution. Electrochemical performance of S-MXene a) CV at 2, 5, 10, 20, 50, and 100 mV/s scan rates, b) GCD plots measured at 0.1, 0.2, 0.3, 0.5, 0.6, 0.8 and 1 A g^{-1} current densities, electrochemical performance of D-MXene c) CV at 2, 5, 10, 20, 50, and 100 mV s^{-1} scan rates, d) GCD plots measured at 0.1, 0.2, 0.3, 0.5, 0.6, 0.8 at 1 A g^{-1} current densities, e) specific capacitance comparison of S-MXene and D-MXene, and f) Electrochemical impedance spectroscopy (EIS) of S-MXene and D-MXene in 1 M Na_2SO_4 electrolyte, (inset) the circuit used for modeling, where R_s: solution resistance, C_{dl}: double layer capacitance at the electrode surface, R_{ct}: charge transfer resistance, Z_w: Warburg resistance. The steeper slope of S-MXene indicates ideal capacitive behavior. The GCD plots were used to calculate specific capacitance for both the MXenes. S-MXene showed superior performance.

Table S6. EIS data obtained for both S-MXene and D-MXene in 1 M Na_2SO_4

	Material	
Component values obtained	**S-MXene**	**D-MXene**
R_s	32.4 Ω	20.7 kΩ
C_{dl}	39.2 nF	12.7 nF
R_{ct}	208 Ω	60.5 kΩ
Z_w	8.01 $nMhos^{1/2}$	987 $nMhos^{1/2}$

Table S7. EIS data obtained for both S-MXene and D-MXene in PBS electrolyte

Material		
Component values obtained	**S-MXene**	**D-MXene**
R_s	168 Ω	192 Ω
C_{dl}	25 µF	2.36 µF
R_{ct}	500 Ω	700 Ω
Z_w	7.69 $nMhos^{1/2}$	5.95 $nMhos^{1/2}$

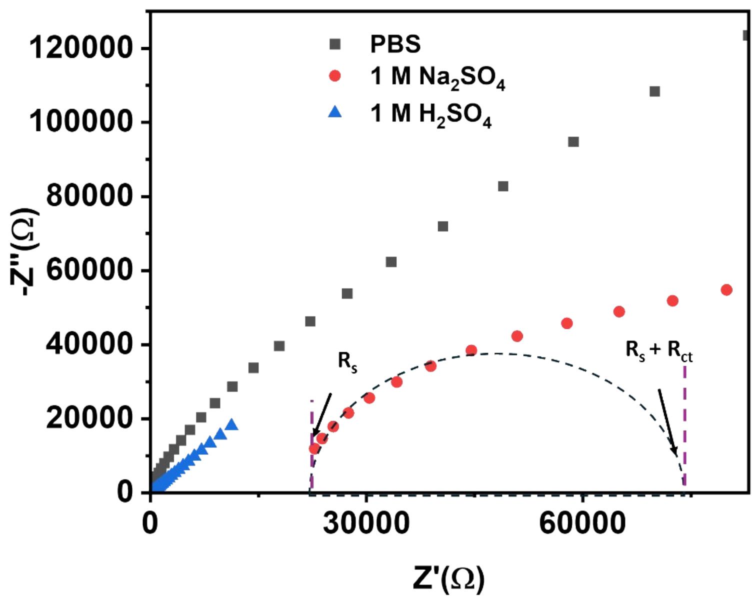

Figure S7. Electrochemical impedance spectroscopy (EIS) of D-MXene in all three electrolytes. A higher starting position of the circle and a higher intercept explain the highest values of R_s and R_{ct} measured at 1 M Na_2SO_4 electrolyte.

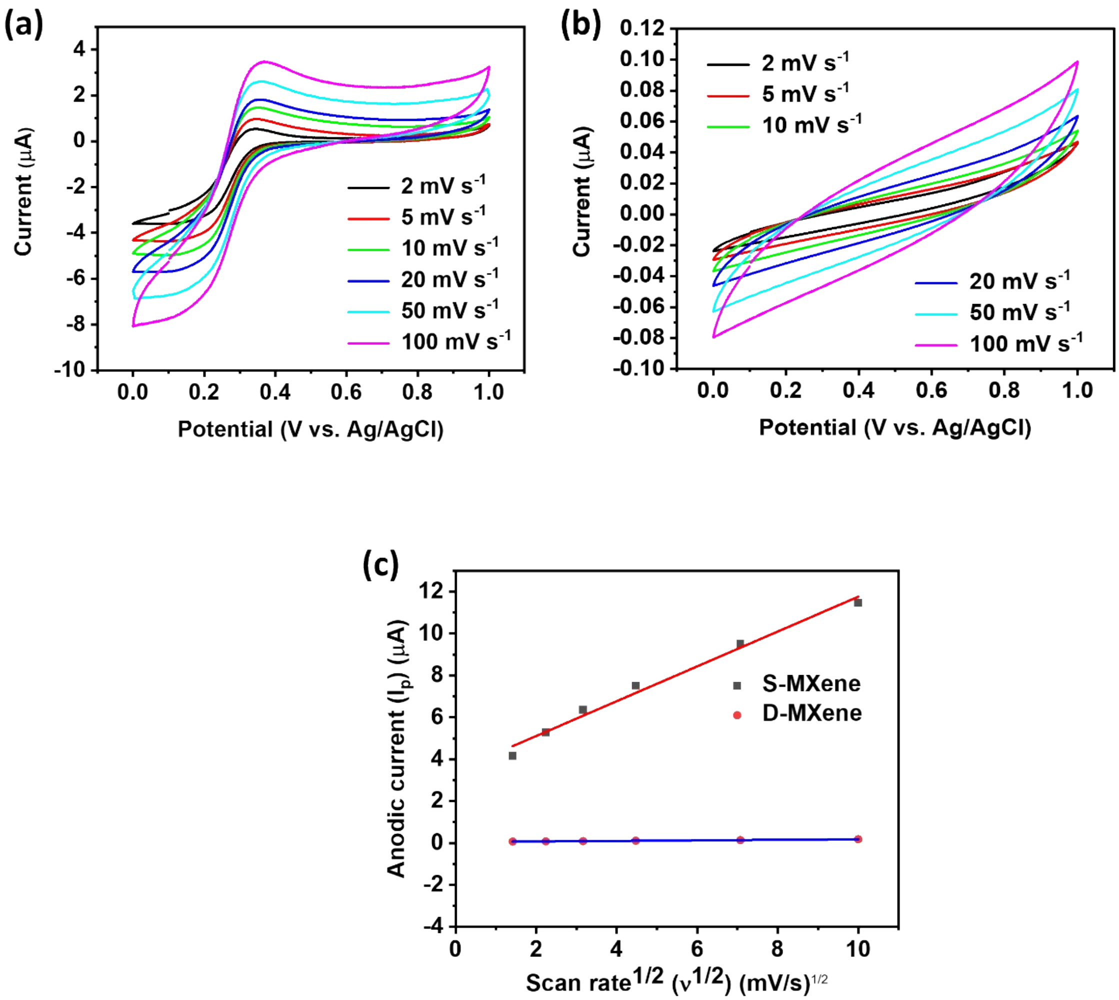

Figure S8. CV plot of a) S-MXene, b) D-MXene, and c) I_p vs $\upsilon^{1/2}$ plot for both the MXenes in 5 mM $K_3[Fe(CN)_6]$ in 1 M KCl solution. The ECSA for S-MXene is higher for D-MXene.

Table S8. Specific capacitance of the supercapacitor device in terms of its mean and standard deviation

Current density (mA cm^{-2})	Specific capacitance (mF cm^{-2})
0.1	87.54 ± 2.88
0.2	77.27 ± 3.58
0.3	72.42 ± 0.92
0.5	65.50 ± 2.44
0.6	61.46 ± 2.01
0.8	58.38 ± 6.54
1.0	54.99 ± 8.96

Table S9. Comparison of available literature using aqueous electrolyte with this work shows the values of energy and power density obtained

Active material	Potential window (V)	Energy density	Power density	Electrolyte	Reference
TiN/Stainless steel (Asymmetric)	1.0	1.614 μW h cm^{-2}	49.98 mW cm^{-2}	PBS	[4]
NbN-TiN (Asymmetric)	0.6	1.86 μW h cm^{-2}	239.14 mW cm^{-2}	PBS	[5]
CNT+PEDOT : PSS (Symmetric)	0.8	0.82 μW h cm^{-2}	2149.8 μW cm^{-2}	PBS	[6]
S-MXene	**0.5**	**2.97 μW h cm^{-2}**	**500 μW cm^{-2}**	**PBS**	**This work**

Table S10. Comparison of power densities for supercapacitors working on all-solid electrolytes

Active material	Biocompatibility of active material	Electrolyte	Biocompatibility of electrolyte	Power density	Reference
Graphene-welded activated carbon	-	polyvinylidene fluoride-hexafluoropropylene + $EMIMBF_4$	-	70 kW kg^{-1}	[7]
CNT/MnO_2	-	Na_2SO_4/Xanthene gum	-	2300 μW cm^{-2}	[8]
Activated carbon	-	etraglyme(G4)/lithium salt (LiTFSI)/ionic liquid (EMIM-TFSI) mixture (GLE)	-	875 W kg^{-1}	[9]
Activated carbon	-	1.3-dimethylimidazolium bis(trifluoromethyl sulfonyl)imide (DMImTFSI)	-	874.8 W kg^{-1}	[10]
V_2O_5	-	PVDF-HFP-PC-		2.3	[11]

		$Mg(ClO_4)_2$		kW kg^{-1}	
$Ti_3C_2T_x$ MXene	Biocompatible	Phosphate buffer saline (PBS)	Biocompatible	500 µW cm^{-2}	**This work**

Table S11. Energy and power density comparison of self-powered implantable medical devices

Configuration	Energy density	Power density	Reference
Piezoelectric nanogenerator	-	68 ± 2.82 µW cm^{-3}	[12]
Piezoelectric nanogenerator	-	22.5 µW cm^{-2}	[13]
Piezoelectric nanogenerator	-	3.75 µW cm^{-2}	[14]
Piezoelectric nanogenerator + supercapacitor	125.4 Wh kg^{-1} (for supercapacitor)	1200 W kg^{-1} (for supercapacitor)	[15]

References:

1 Y. Sheng, X. Tang, E. Peng and J. Xue, *J. Mater. Chem. B*, 2012, **1**, 512–521.
2 A. Pazniak, P. Bazhin, N. Shplis, E. Kolesnikov, I. Shchetinin, A. Komissarov, J. Polcak, A. Stolin and D. Kuznetsov, *Mater. Des.*, 2019, **183**, 108143.
3 E. M. López-Alejandro, E. Ramírez-Morales, M. C. Arellano-Cortaza, C. A. Meza-Avendaño, D. M. Frías-Márquez, R. Ramírez-Bon and L. Rojas-Blanco, *Ceram. Int.*, in press.
4 S. Sharma, R. Adalati, M. Sharma, S. Jindal, A. Kumar, G. Malik and R. Chandra, *Ceram. Int.*, 2022, **48**, 34678–34687.
5 S. Sharma, R. Adalati, N. Choudhary, B. Unnikrishnan, M. Sharma, P. Gopinath and R. Chandra, *J. Alloys Compd.*, 2023, **960**, 170749.
6 H. J. Sim, C. Choi, D. Y. Lee, H. Kim, J.-H. Yun, J. M. Kim, T. M. Kang, R. Ovalle, R. H. Baughman, C. W. Kee and S. J. Kim, *Nano Energy*, 2018, **47**, 385–392.
7 C. Li, X. Zhang, Z. Lv, K. Wang, X. Sun, X. Chen and Y. Ma, *Chem. Eng. J.*, 2021, **414**, 128781.
8 N. Yu, X. Wang, S. Zhang, S. Zeng, Y. Zhang, J. Di and Q. Li, *RSC Adv.*, 2019, **9**, 8169–8174.
9 D. Lee, Y. H. Song, U. H. Choi and J. Kim, *ACS Appl. Mater. Interfaces*, 2019, **11**, 42221–42232.
10 X. Zhong, J. Tang, L. Cao, W. Kong, Z. Sun, H. Cheng, Z. Lu, H. Pan and B. Xu, *Electrochim. Acta*, 2017, **244**, 112–118.
11 A. Jain, S. R. Manippady, R. Tang, H. Nishihara, K. Sobczak, V. Matejka, M. Michalska, *Sci. Rep.*, 2022, **12**, 21024.
12 S. Azimi, A. Golabchi, A. Nekookar, S. Rabbani, M. H. Amiri, K. Asadi and M. M. Abolhasani, *Nano Energy*, 2021, **83**, 105781.
13 Y. Zhang, L. Zhou, C. Liu, X. Gao, Z. Zhou, S. Duan, Q. Deng, L. Song, H. Jiang, L. Yu, S. Guo and H. Zheng, *Nano Energy*, 2022, **99**, 107420.
14 Q. Shi, T. Wang and C. Lee, *Sci. Rep.*, 2016, **6**, 24946.
15 P. P. Singh, S. K. Si and B. B. Khatua, *Chem. Eng. J.*, 2025, **511**, 161802.